NAWI Graz
Natural Sciences

TU Graz

Verena Fritz, BSc

Measuring Temperatures on a TEM sample using Parallel Beam Electron Diffraction

Master's Thesis

to achieve the university degree of

Diplom-Ingenieurin

Master's degree programme: Technical Physics

submitted to

Graz University of Technology

Supervisor

Ao. Univ.-Prof. Dipl-Ing. Dr.techn. Werner Grogger

Co-Supervisor

Dipl-Ing. Robert Krisper

Institute of Electron Microscopy and Nanoanalysis

Graz, August 2021

Affidavit

I declare that I have authored this thesis independently, that I have not used other than the declared sources/resources, and that I have explicitly indicated all material which has been quoted either literally or by content from the sources used. The text document uploaded to TUGRAZonline is identical to the present master's thesis.

<div>

Date   Signature

</div>

Abstract

Parallel beam electron diffraction (PBED) can be used to determine the temperature from the thermal expansion of a material via its diffraction pattern. As such, it can be used to measure the local temperature in an *in-situ* heating experiment. This approach should, in principle, be feasible in any well aligned microsope with a camera. Despite its general applicability, so far, precise measurements have only been performed in high-end TEMs.

For TEMs with 2 condenser lenses, we show how to align the microscope for a parallel electron beam - which is a crucial prerequisite for the measurement. Moreover, in order to achieve satisfactory results even with lower camera resolutions of 1 megapixel, a sophisticated evaluation algorithm is developed. Using the latter we are able to demonstrate the possibility of determining the diffraction ring radii of Au nanoparticles to within 0.04 pixel and therefore measure the temperature of a given sample to an accuracy of approximately 6 °C.

Kurzfassung

Mit der Parallelstrahl-Elektronenbeugung (PBED) kann die thermische Ausdehnung eines Materials über dessen Beugungsmuster bestimmt werden. Ist der thermische Expansionskoeffizient des Materials bekannt, so kann diese Methode zur Messung der lokalen Temperatur in einem *in situ* Heizexperiment herangezogen werden. Ein Vorteil dieser Methode ist, dass sie in jedem Mikroskop verwendet werden kann, das mit einer Kamera ausgestattet ist und die Ausrichtung der Linsen für einen parallelen Elektronenstrahl ermöglicht. Trotzdem wurden präzise Messungen bisher nur in High-End-TEMs durchgeführt.

Für TEMs mit zwei Kondensorlinsen zeigen wir, wie man das Mikroskop für einen parallelen Strahl einstellt - was eine entscheidende Voraussetzung für die Messung ist. Um auch bei geringeren Kameraauflösungen von 1 Megapixel zufriedenstellende Ergebnisse zu erzielen, wird zudem ein ausgeklügelter Auswertealgorithmus entwickelt. Mit diesem demonstrieren wir die Möglichkeit, die Beugungsringradien von Au-Nanopartikeln auf 0.04 Pixel genau zu bestimmen und damit die Temperatur der Probe mit einer Genauigkeit von bis zu 6 °C zu messen.

Acknowledgements

At this point, I would like to express my gratitude to all those who have accompanied me on my way to this point.

Starting with my supervisor, Prof. Werner Grogger, whom I would like to thank for his guidance and patience. He always asked the right questions during meetings and made sure that the project stayed on track. Great thanks are also due to co-supervisor Robert Krisper. He was always available to answer questions, made sure I had everything I needed for the experiments, and was a great help in structuring the thesis in the best possible way.

Furthermore, I would like to thank Prof. Ferdinand Hofer, the (now former) head of the institute, who gave me the opportunity to write my master thesis at the Institute of Electron Microscopy and Nanoanalytics.

I want to express my gratitude towards the whole Felmi-ZFE team for creating such a pleasant working atmosphere. Especially the TEM group for the (pre-covid) daily meetings that kept me motivated. I would especially like to thank Ilse Letofsky-Papst for instructing me on the T12 and Stefan Mietsche for the supportive XRD measurements.

Also, thank you to my fellow thesis students, Anas, Alex, Michi, Nik, Benni, Jakob, Michele and Moritz, for the fun "Diplomandenabende".

Moving on to the people who supported me outside the Felmi-ZFE: I would like to express a special thanks wrapped in a big hug to my friends and fellow physics students who have accompanied my way since the first semester: Flo, Martin, Stef, David, Hannes and Christian. Although we all went to different fields of physics, we have always stayed connected and conquered many adventures (besides uni) together.

A massive thank you goes to my boyfriend Christian. He has played a huge role in my development as a student and scientist and always challenges me to question every last detail of my research.

Finally, I would like to thank my family - first and foremost my mother, my grandma, and Max - for their constant support and for always being my calm harbor.

Contents

1. Motivation

In *in-situ* experiments, the response of a sample to a specific stimulus - such as heating - can be observed in real time. Over the last decade, the field of TEM *in-situ* heating experiments has been revolutionized by the introduction of microelectromechanical (MEMS) based heating systems. Due to the small size of MEMS-based heating elements, rapid temperature changes and high stability can be achieved. This opens the door to high-resolution observations of thermally initiated processes on the micro- and nanoscale.

What remains a challenge, however, is the accurate determination of the sample temperature. While the MEMS system outputs the overall temperature of the heating element it relies on external calibration and its error increases with temperature. In addition, it would be desirable to resolve the temperature locally, since the sample geometry and composition can lead to an non-uniform heat distribution and the electron beam may additionally heat the sample.

Therefore, an *in operando* measurement method is sought that allows us to resolve the temperature locally and accurately. For example, one can infer the temperature of a material from its thermal expansion. In the work of Niekiel et al. [1] it was shown that the determination of this thermal expansion by parallel beam electron diffraction (PBED) provides a sound method for temperature measurements in the TEM. Unlike other methods, PBED does not require a spectrometer, so it can be used in most electron microscopes. However, it is emphasized that the high accuracy of this technique is mainly enabled by the high-end three-condenser-lens system of the used microscope and its camera with a resolution of $2048 \times 2048\,\mathrm{px}$.

The central question of this work is therefore whether we can extend the scope of this method to TEMs with 2 condenser lenses and a lower resolution camera. Since several factors influence the accuracy of the PBED temperature measurement, we can tackle the problem on multiple fronts: the material used, the alignment of the parallel beam (as a prerequisite for accurate measurements) and - most importantly - the evaluation of the diffraction patterns. Thus, as a final product, we would like to establish a routine for PBED

temperature measurements that can be used in "everyday" *in-situ* heating experiments.

2. Temperature measurement methods

In this chapter, we introduce the heating system used to perform *in situ* heating experiments, followed by an overview of the state of the art in TEM temperature measurements. We then focus on the method used in this work (PBED) and take a closer look at the parallel electron beam. At the end of this chapter, we consider which materials are suitable and available for such a measurement.

2.1. *In situ* heating experiments

In the last decade, a lot has happened in the field of TEM *in situ* heating experiments due to the introduction of MEMS-based heating systems. In Figure 2.1 we see a side-by-side comparison of a conventional TEM grid and a MEMS based *Nano-Chip*, as well as the corresponding TEM holders. Compared to furnace based holders, the MEMS system has many advantages [2]:

- Due to its small dimensions it needs much less power.
- It does not require cooling of the surrounding parts of the chip and holder.
- We can achieve very high heating and cooling rates.
- The induced sample drift is very low.
- It offers the possibility to combine the heating measurement with an electrical bias of the sample.
- It allows for EDS analyses at elevated temperatures.

The heating and temperature measurement with the MEMS system works with the 4-point probes method: a known electric current flows through the spiral via the two outer contact pads of the *Nano-Chip*. The voltage dropping across the spiral is tapped at high impedance via the two inner contact pads
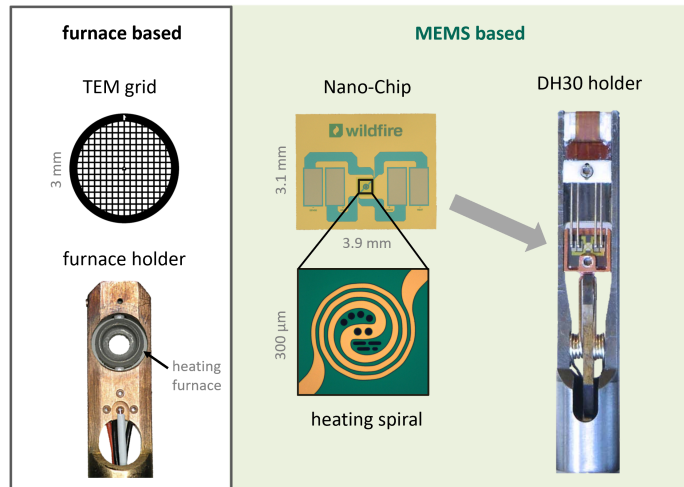
Figure 2.1.: **furnace based**: A conventional TEM grid is placed in a furnace based heating holder [2]. **MEMS based**: The MEMS *Nano-Chip* has a heating spiral with electron transparent windows in the center. On the right side we see the tip of the heating holder with the already mounted *Nano-Chip*, which is contacted on the four rectangular pads [3].

and measured with a voltmeter. The resistance is calculated from Ohm's law and is related to the temperature via the Callendar Van Dusen equation [3]:

$$R(T) = aT^2 + bT + c \tag{2.1}$$

Below 800 °C the quadratic term is negligible leaving us with a linear relation, where the offset c is the resistance at $T = 0$ °C. To get the slope b, we need the resistance of the heating spiral at room temperature and a calibration factor that is stated on the box (see Fig. 2.2).

As we can see, several chips (here e.g. ten) come in a box with the same calibration factor. Since the chips belong to the same production batch, it is assumed that the heating spirals all have approximately the same layer thicknesses and thus the same resistance. In case b deviates slightly from the real value of the individual chip, we can see from Eq. (2.1) that the error will increase linearly with increasing temperature. For the *DENSsolution Wildfire* MEMS system in Fig. 2.1 this error is 5 % of the displayed temperature [3]. Therefore, if samples are examined at high temperatures, greater deviations from the actual temperature must be expected.

Figure 2.2.: Box of *Nano-Chips*. The ones we are using are covered with a $<20\,\text{nm}$ thick SiN_x membrane. On the label the coefficients a and b for Eq. (2.1) are given.

The exact specifications of the equipment used for the experiments in this thesis can be found in Chapter 4.

2.2. Overview of available methods

Measuring the temperature of a TEM sample during an *in situ* experiment is a challenging task, but there are multiple approaches and methods to do so. This section provides a short overview of available methods (see Fig. 2.3) following the review article by Gaulandris et al. [2].

A distinction is made between continuous methods, in which any temperature can be measured over a wide range, and material-specific reference points, in which a visible change in the sample can be assigned to a specific temperature. Such reference points can be used to calibrate a continuous temperature measurement.
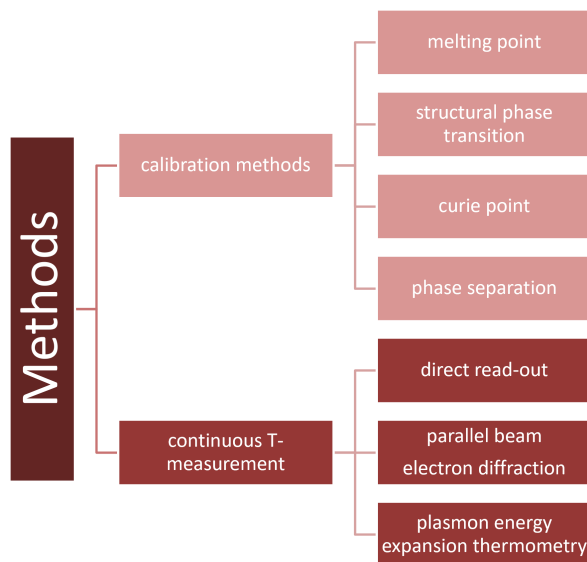

Figure 2.3.: Techniques for the continuous measurement of temperature in the TEM, and calibration methods using various types of reference points.

In the following we will provide a short description of the calibration methods. An overview of materials that have been successfully used for these methods can be found in [2].

Melting point
When a material goes from solid to liquid, it loses its ordered crystal structure. This can be exploited for temperature measurements through imaging and

diffraction techniques.

Melting points of bulk materials are usually well characterized in the literature. However, the melting temperature of nanoparticles is lower than for the bulk material due to the larger surface-to-volume ratio [4]. Therefore, less thermal energy is required to release an atom from a solid [5].

While the melting point of a particle of certain size can be calculated theoretically [6], nanoparticles are highly mobile at elevated temperatures and may not adhere to a substrate long enough for a thorough experimental validation of said calculations.

Structural phase transition

Structural changes in the crystal can be detected in the TEM from the diffraction pattern or with HRTEM imaging [7],[8]. Since the TEM operates in high vacuum, we are only interested in materials that have pressure independent phase transitions. However, the preparation of such samples is often complicated due to their complex composition or sample geometry. Moreover, in the case of nanoparticles, the increased mobility at high temperatures can lead to a rotation of the nanoparticles out of the zone axis, which could be misinterpreted as a phase transition.

Curie point

The Curie point in ferro- (and ferri-) magnetic materials can also serve as a reference point. In the TEM, the magnetic moment of the sample causes an image shift. This fact can be used to detect the Curie point as follows: At different temperatures, one image is taken in focus and one in overfocus. The shift between those two images will become zero once the Curie point is reached [9].

For this measurement, a furnace based holder would be beneficial, as it is important that the sample is well secured. The forces between the magnetic sample and the magnetic field of the objective lens can otherwise cause it to be pulled out.

Phase separation

An alloy can dissolve into phases of the metals it consists of. This separation process can be observed in the TEM and can be assigned to a specific temperature - described by the solvus line in the phase diagram. As is often the case, it is questionable whether the TEM sample is representative of the bulk material. It is not clear whether the sample has the same overall composition as the bulk alloy, for which the solvus line is well defined [10].

Now we will briefly introduce the continuous methods. PBED is excluded for now, but will be discussed in detail in the next section.

Direct read-out
Most heating holders have a read-out function that gives back the current temperature. For furnace based holders this works via a thermocouple mounted directly on the holder, while for a MEMS-based system, we obtain the resistance $R(T)$ from the 4-point probe measurement. A disadvantage of the latter is that the uncertainty increases with temperature (see Section 2.1), which is of course inconvenient if you are interested in the behavior of a material at high temperatures. Moreover, such direct read-outs only give an average temperature. However, the support film or parts of the examined sample can have a lower temperature than the heating element due to their low thermal conductivity.

While it is convenient to be able to read the temperature directly from the fixture, it is important to be able to validate it and, furthermore, resolve it locally.

Plasmon energy expansion thermometry (PEET)
An electron in the beam can lose energy as it passes through the sample by creating a charge oscillation - called a plasmon - in the material. The energy of such plasmons is proportional to the square root of the electron density in the material. Therefore, as the material expands from an increase in temperature, the decrease in electron density can be seen in the electron-energy-loss-spectrum (EELS) [11],[12].

With this method it is possible to resolve the temperature down to nanometer scale. However, it is of course tied to TEMs that offer the possibility of EELS measurements.

2.3. Measuring temperature with PBED

Most materials have a positive thermal expansion coefficient α, i.e. they expand when heated. The larger α, the more the average distance between atoms increases with temperature. This relationship is linear to a good approximation for many materials [13].

$$\frac{d(T)}{d_0} = 1 + \alpha(T - T_0) \qquad (2.2)$$

d stands for the distance between lattice planes, the slope α is the thermal expansion coefficient (TEC), and T_0 is the reference temperature.
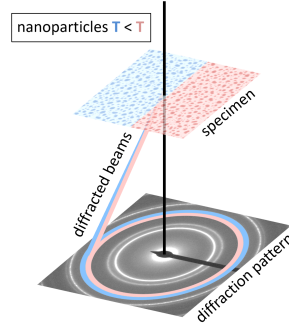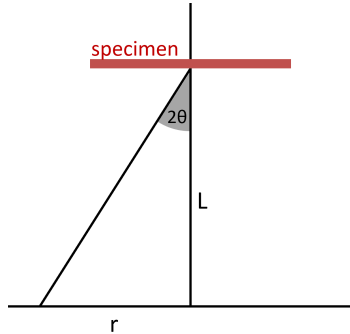

Figure 2.4.: PBED

As the material expands, we see a contraction of the diffraction pattern in the TEM. For a polycrystalline material, this means that the diffraction rings decrease in diameter as T increases.

In Figure 2.5 we see the ray diagram of an electron beam diffracted at an angle 2Θ. In the plane of the diffraction image, the beam hits the screen at a distance r from the undiffracted beam. From the Bragg equation and the geometry of the ray diagram, we derive Equations (2.3).

$$\frac{r}{L} = tan(2\theta) \approx 2\theta$$
$$\lambda = 2dsin\theta \approx 2d\theta$$
$$\frac{\lambda}{d} \approx 2\theta \approx \frac{r}{L} \qquad (2.3)$$
$$rd = \lambda L$$

Figure 2.5.: Ray diagram

Now we can rewrite Equation (2.2) linking the radius of the diffraction rings to the TEC.

$$\frac{r_0}{r(T)} = 1 + \alpha(T - T_0) \qquad (2.4)$$

9

The right hand side of the equation stayed the same and again, the slope α equals the TEC.

2.3.1. Parallel illumination

As the name of the method implies, the measurement is conducted with a parallel electron beam. However, there are three angles of inclination (α, β, ϕ) that contribute to the non-parallelism of the beam, each having different origins [14].
In Figure 2.6 we see those angles visualized in ray diagrams.

- A certain point on the sample is hit by electrons coming from different angles. This range of incident angle is called $\boxed{\alpha}$ and it results from the finite size of the crossover above the objective lens. This ultimately results from the finite size of the electron source.
- $\boxed{\beta}$ is the convergence angle. It is the variation in mean incident angle over the entire illuminated area. We can adjust β by changing the excitation of the condenser lenses. When exciting them more, the beam will spread out, for low lens currents the beam will be more focused.
- As the electrons pass through the magnetic lenses, they are forced onto a spiral path by the Lorentz force. This causes an inclination $\boxed{\phi}$ of the electron path relative to the sample.
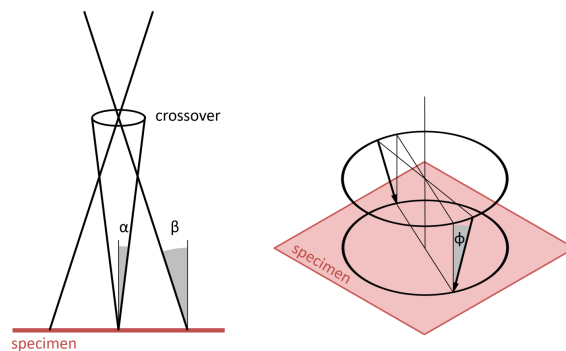

Figure 2.6.: The three inclination angles α, β and ϕ contributing to the non-parallelism of the electron beam.

Although we can adjust the radial components α and β to be very small, the tangential part ϕ will always remain. However, since we are dealing with

polycrystalline samples and thus with radially symmetric diffraction patterns, we do not need to consider this.

The reason it is important to have a parallel beam is that the heater chip bulges. The center part of the chip itself expands from the temperature increase, but since its surrounding does not, it will start to bulge - effectively moving the sample slightly upwards in the TEM column. In imaging mode, this change in height will become apparent as the sample moves out of focus.

However, it is not only disturbing the heating experiment in imaging mode: for a non-parallel beam the ring radii of the diffraction pattern change their diameters (see Fig. 2.7). Since the change in diffraction ring radii is also what the entire PBED temperature measurement is based on, bulging of the chip would greatly interfere with our measurement. However, if we can tune the convergence angle β to be close to zero, the effect of bulging on the ring radii will become negligible.
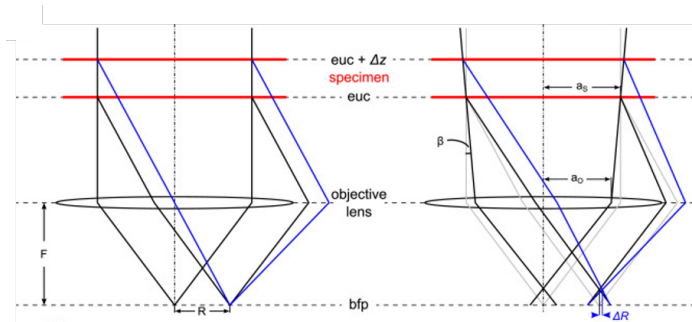

Figure 2.7.: For a non-parallel beam, a change in z-height of the sample will result in a change in the diffraction ring radius ΔR. Image from Niekiel et al. [1]

This means that we have to find lens settings that result in a parallel beam. Here it makes a big difference whether the TEM used is equipped with two or three condenser lenses. The three condenser lens TEM (i.e. used by Niekiel et. al. [1]) has the advantage of the so-called *C2/C3 zoom* which simplifies the search for the parallel beam settings.

To find the correct lens settings for two condenser lenses, a sample is moved up and down in the TEM. If the ring radii of the diffraction pattern do not change despite the change in height, we have a parallel electron beam. How this preparatory experiment proceeds in detail will be explained in Section 4.3.

2.3.2. Choice of materials

In order to be able to measure the temperature from the diffraction pattern the material used must meet several criteria:

- **large thermal expansion coefficient**
- **high melting point**
- stability in the electron beam
- insensitivity to transfer (oxidation in air)

The first and most important point on the list is that the material expands as much as possible, so that there is a measurable difference in the diffraction patterns. After all, the more it expands the better the resolution of the temperature measurement will be in the end. Furthermore, we want it to have a high melting point, so it provides a wide temperature range to measure over.
There are several materials that fulfill these two requirements but most of them bring some issues to the table when it comes to sample preparation or their stability when exposed to the electron beam. The choice of suitable materials is further narrowed down by the condition that the material must be chemically inert, so that only thermal expansion changes the lattice parameter. Moreover, it must be stable in the vacuum of the TEM and produce a nicely defined diffraction pattern.

In sample preparation, the question is whether to have the materials as a a thin layer or rather as nanoparticles on the chip. The former would provide more signal because more electrons are scattered, making it easier to evaluate the more clearly defined diffraction rings. On the other hand, however, nanoparticles are free to expand in all directions and we would not have to worry about inducing stress in the sample as the temperature increases.

In Table 2.1, we see the prime candidates. Au is the safest bet, since it has proven to be easy to handle and stable throughout many measurements in the work of Niekiel et al. [1]. Ag and Al have also been used for PBED temperature measurements in literature, however Ag was used in an Environmental TEM (ETEM) under H_2 atmosphere and Al was deposited as a thin layer instead of nanoparticles [15],[16].

Table 2.1.: Materials and the criteria for a successful PBED temperature measurement.

material	α [10^{-6} K^{-1}]	melting point [°C]	no oxidation	reference
Au	14.2	1,064	✓	Niekiel et al. [1]
Ag	18.0	962	✓	Winterstein et al. [15]
Al	23.1	660	✗	Cremons et al. [16]
Cu	16.7	1,084	✗	

The problem with Al is that with our heating holder we cannot prepare and measure the sample without ever exposing it to air where it would oxidize to an uncertain degree. A partially oxidised sample does not necessarily have the same thermal expansion coefficient as bulk aluminium. For the PBED temperature measurement, however, it is of utmost importance to know the exact thermal expansion coefficient.

3. Evaluation of diffraction patterns

In the previous section we discussed how an increase in temperature manifests itself in the decrease of the diffraction ring radii. As we can see in Figure 3.1, the ring radii change only by a few pixels even for a large temperature difference. With Au nanoparticles, for example, a 100 °C temperature difference makes only 0.5 pixel difference in the ring radius of the (220) diffraction ring.

Therefore, it is of utmost importance to have a very precise evaluation algorithm. In a nutshell, the evaluation consists of two major steps: First, the DP is integrated azimuthally around its center to obtain the radial profile. In a second step we can extract the ring radii by fitting the peaks.
Although this sounds like a simple 2-step plan, it is a difficult endeavor to achieve high accuracy. The integration center must be determined to within a fraction of a pixel to avoid falling victim to pixel artifacts later. Another hurdle is the fit of the radial profile: We have to decompose it into the contributions from the nanoparticles, the membrane of the support grid and the undiffracted (zero) beam.
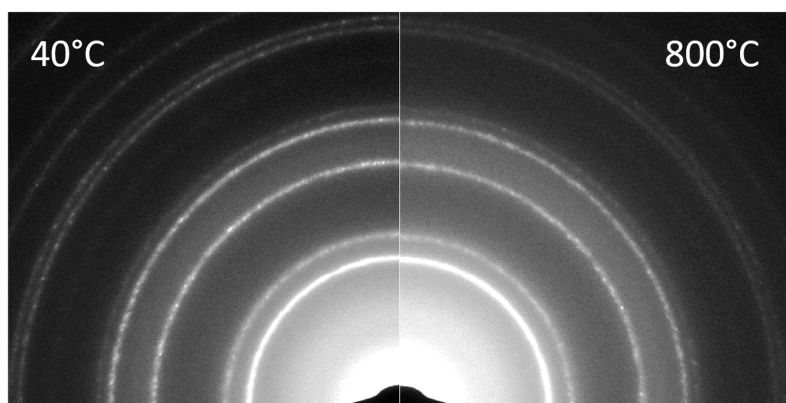

Figure 3.1.: Side-by-side comparison of DPs of Ag nanoparticles at 40 °C and 800 °C.

3.1. Localizing the center of the diffraction rings

As already emphasized, the center of the diffraction rings must be determined very precisely. However, in the recorded diffraction images the center is concealed by the beam stop, to protect the camera from overexposure by the undiffracted beam (see e.g. in Fig. 3.4(a)). Therefore, we must find a way to determine the center indirectly via the rings.

In this section we present three algorithms to do so. Two of them are from literature and the third one, called Peakmax, is an original creation. We discuss their efficiency and accuracy and decide which one is best suited for the application on diffraction rings.

3.1.1. Circular Hough Transform

The Circular Hough Transform (CHT) algorithm can effectively find circles in an image and, consequently, their center.
First, the features we are interested in are isolated by thresholding. To do so, the pixels that form the diffraction ring are set to an intensity value of 1, while all other pixels are set to zero (Fig. 3.2a). Now we draw so called Hough circles from each of the non-zero pixels. All of these circles have the same radii. If those radii are the same as the radius of the diffraction ring, there will be a maximum overlap of the Hough circles at the position of the diffraction ring center (Fig. 3.2c). Since the radius of the diffraction ring is unknown, we have to gradually increase the Hough circle radii until we achieve maximum overlap (Fig. 3.2).

For a precise determination of the center, we need to try out many different radii for the Hough circles. Even if we restrict the radius range, the method remains computationally expensive. There is a script for DigitalMicrograph that is optimized specifically for diffraction rings [17]. While there are also packages available for Python and Matlab, they are primarily intended for the rough location of round structures and do not provide the accuracy we are aiming for.
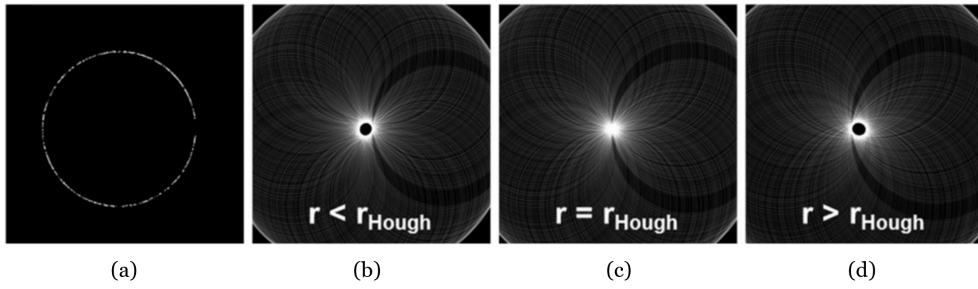
16

(a) (b) (c) (d)

Figure 3.2.: (a) Diffraction ring after thresholding. (c) When the circles drawn from each non-zero pixel have a radius $r = r_{Hough}$ there is a maximum overlap of all circles in the center of the diffraction ring.
Reprinted from Cremons et al. [16] with permission from Elsevier.

3.1.2. Cross-correlation

Cross-correlation is often used when you need to find a particular feature in an image [18]. In our case, we want to find a ring and thereby its center. The cross-correlation between an input x and a kernel w in two dimensions is given by

$$y(i, j) = \sum_m \sum_n x(m - i, n - j) w(m, n). \tag{3.1}$$

Figure 3.3 illustrates what happens in Equation (3.1): The kernel is dragged across the input matrix. At each position, the superimposed entries are multiplied and the resulting products are summed up.
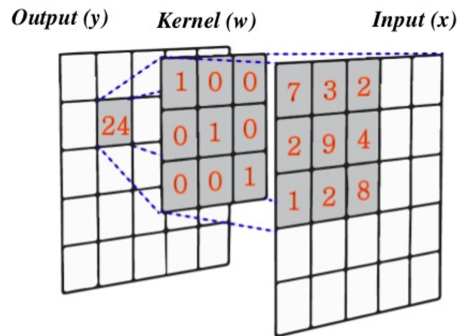

Figure 3.3.: Schematic operation of the 2D cross-correlation.

To use cross-correlation for our purposes, we define the DP as the input and

for the kernel we construct a zero-matrix with with a ring of ones (Fig. 3.4(a,b)). We choose the size of the kernel-ring to match the most pronounced ring of the DP. The output y (Fig. 3.4c) will have its maximum when the kernel-ring lies centered on top of the diffraction ring. Then we can safely say that the center of the-kernel ring is at the same location as the (up to now unknown) center of the DP.

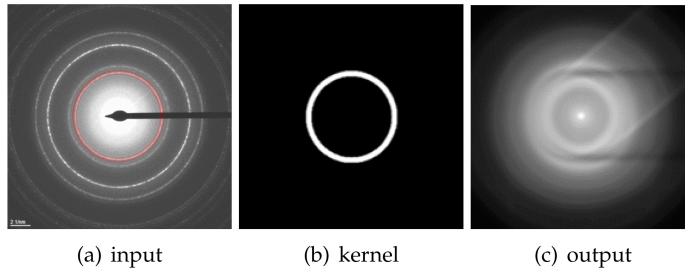| (a) input | (b) kernel | (c) output |

Figure 3.4.: Cross-correlating a DP (a) with a ring (b) gives an output matrix (c) that has a maximum at the position of the center. The most pronounced ring of the DP is highlighted in red.

This algorithm gives us the pixel that most likely inhabits the center. Cross-correlation is available as `scipy.signal.correlate` in Python and while this operation is not very time consuming, it can be sped up by cropping the input and kernel images so they only include the relevant ring.

Subpixel accuracy

Unfortunately, the accuracy of the conventional cross-correlation is not sufficient for our purposes. To determine the center more precisely, we first need to upsample the DP using Python's `scipy.ndimage.zoom`. This scales up the dimensions of the DP as follows:

$$new\ dimensions = old\ dimensions * zoom\ factor.$$

The newly introduced pixels in between are filled using spline interpolation and the size of the kernel is adjusted accordingly. We can now perform a cross-correlation of these enlarged arrays and therefore calculate the center with sub-pixel accuracy for the original size of the DP.
With a zoom factor n we get a result accurate to $\frac{1}{n}$ pixel. Of course, this also means that the computational effort of the operation scales quadratically with the zoom factor and thus also with the precision of the method.

3.1.3. Peakmax method

When we compute the radial profile, we integrate azimuthally around the center of the DP. In Figure 3.5 we see how the radial profile changes as we move the integration center away from the center of the DP. We notice that the farther they are apart, the broader and smaller the peaks will become. At some point they even split into two peaks.
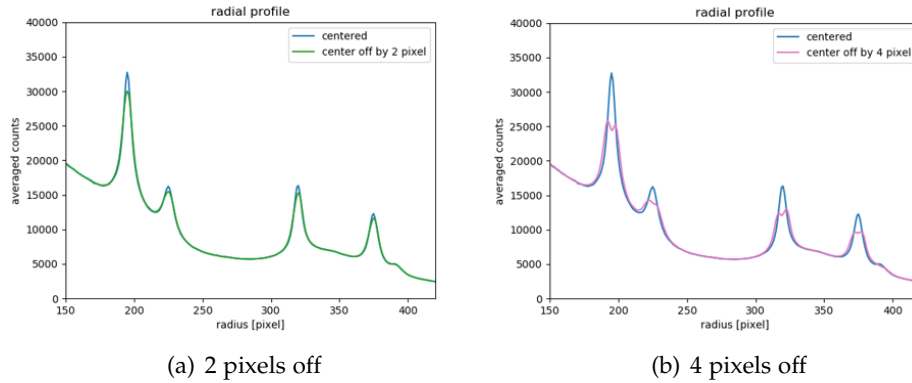

(a) 2 pixels off (b) 4 pixels off

Figure 3.5.: Radial profiles of a DP where the integration center does not coincide with the center of the DP.

Looking at it the other way around: the closer we choose the center of the radial profile to the unknown center of the DP, the higher the peaks will be. We can use this observation to find the center coordinates of our diffraction rings:

The peak height h is a function of the integration center with coordinates i, j. By varying i and j we want to find the maximum peak height. We can choose i and j also between the pixels and thus locate the center very precisely. It would, however, be computationally expensive to evaluate the peak height at a large number of points. Therefore, we need to come up with a scheme to find the maximum of $h(i, j)$ in a few steps.

An elegant way to find such a maximum would be a gradient search, also known as "hill climber". Such an algorithm evaluates the local slope at a certain point and then chooses its next step uphill. The step size is adapted to the gradient, i.e. the closer it gets to a maximum, the smaller the steps. In our case, however, it turns out that the function h is not smooth enough, which causes the hill climber to get stuck at a local maximum.

19

This can be circumvented by considering several points instead of just one at each step: We draw a grid of (i, j) values around what we assume to be the center and compute the peak height h for these limited number of points (Fig. 3.6). It will have the shape of a 2D peak, that we can now fit with a 2D Gaussian function given in Eq. (3.2). The maximum of the fit will then tell us the center coordinates.

$$f_X(x_1, x_2) = \frac{1}{2\pi\sigma_1\sigma_2\sqrt{1-\varrho^2}} \exp\left(-\frac{1}{2(1-\varrho^2)}\left[\frac{(x_1-\mu_1)^2}{\sigma_1^2} + \frac{(x_2-\mu_2)^2}{\sigma_2^2} - \frac{2\varrho\,(x_1-\mu_1)\,(x_2-\mu_2)}{\sigma_1\sigma_2}\right]\right)$$

(3.2)

Unlike subpixel cross-correlation, the computational cost of this method does not scale with accuracy.
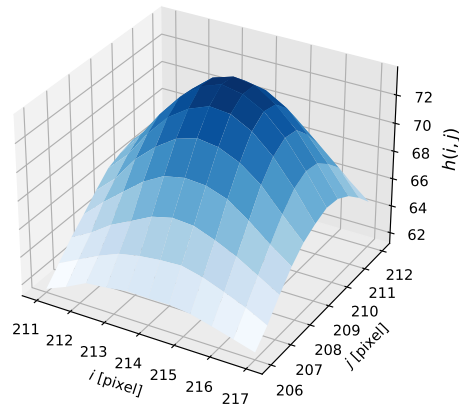

Peak height for a grid of center coordinates

Figure 3.6.: The values for the peak height for different integration center coordinates (i, j) form a 2D peak that can be fitted with a Gaussian.

A cross-correlation and Peakmax hybrid

With common cross-correlation we get to the center quickly but inaccurately (error of ± 1 pixel). Peakmax is costly but allows us to determine the center with high accuracy. To exploit the strengths of both algorithms, we go with a

mixture of both of them.

First, we use cross-correlation to find the center to pixel accuracy. Then, we evaluate the peak height h in the vicinity of this pixel. The number of grid points at which we have to evaluate h can be greatly reduced and we have a very accurate and relatively fast center finding method.

It was observed that slight distortions of the diffraction pattern can affect the determination of the center. This effect can however be mitigated by a correction of the beam stop: After determining the center with pixel accuracy using cross correlation, a slice of the DP containing the beam stop was replaced by a copy of the neighboring slice (Fig. 3.7). This gives us a more continuous (220) ring and the Peakmax method can now find the most probable center coordinates of the diffraction ring.
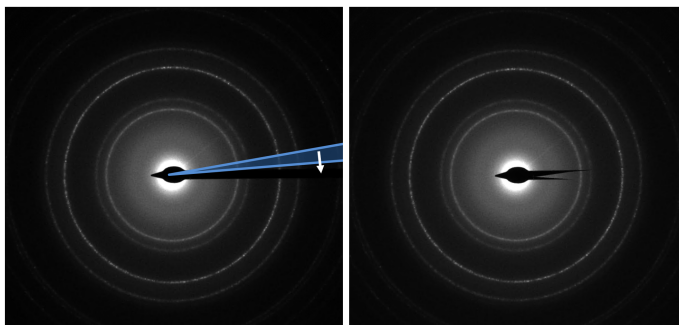

Figure 3.7.: Masking the beamstop with a neighboring slice of the DP for the Peakmax algorithm.

3.2. Fitting the radial profile

Once we have found the center, we can now decompose the radial profile into its components. In this section, we demonstrate this using the example of a sample with Au nanoparticles.

In the radial profile (blue curve in Fig. 3.9), a rapidly decaying background is clearly visible. This fall-off of the zero beam is caused by inelastic scattering and can be fitted from the data in the red marked area. Looking at the DP in Figure 3.8a, we see that the area corresponding to this part is partially covered by the beamstop. To get rid of the influence of the beamstop on the radial profile, we apply a wedge mask (Fig. 3.8b).
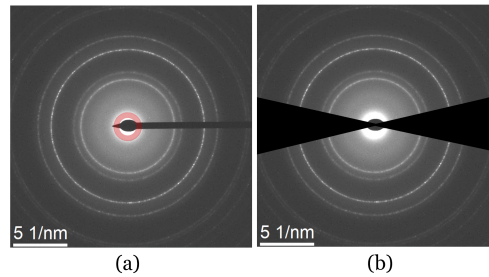
Figure 3.8.: Diffraction pattern of Au NP. (a) The beamstop covers parts of the area that provides the data for the powerlaw fit (red area, also marked in Fig. 3.9). (b) To prevent the beamstop from interfering we mask these parts with wedges.

The background can be fitted with a Powerlaw and subtracted from the radial profile [1]. The resulting yellow curve in Figure 3.9 consists of some very distinct Au peaks sitting on a background of several broad "bumps" originating from the *Nano-Chips* membrane. The membrane consists of amorphous SiN_x and therefore has no long-range order in the atomic lattice. As a result, it produces diffuse diffraction rings - which manifest themselves as relatively broad hills in the radial profile.
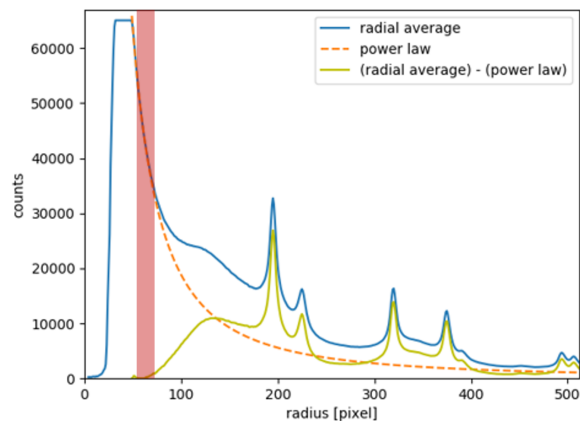

Figure 3.9.: The wedge-corrected radial profile (blue) is broken down into its components: By subtracting the powerlaw fit (orange), we obtain the yellow curve, which still contains a background from the SiN_x membrane.

Ultimately, we want to know the exact location of the Au peaks. Therefore, we must try to deconvolve the yellow curve in Fig.3.9 into its components.
To get a rough idea of how much the SiN_x background effectively shifts the peaks, we can make an estimation: We approximate the Au peak by a parabola

$f(x) = -ax^2$ sitting on a part of the SiN$_x$ bump that has a local slope k and is approximated by a line $g(x) = kx + d$. The question now is by how much the peak position of the overall curve $h(x) = f(x) + g(x)$ differs from the peak position of $f(x)$. To calculate the maximum of $h(x)$, we set its first derivative to zero.

$$h(x) = f(x) + g(x) = -ax^2 + kx + d \tag{3.3}$$

$$h'(x) = -2ax + k \stackrel{!}{=} 0 \;\longrightarrow\; x_0 = k/2a \tag{3.4}$$

This means that the peak of $h(x)$ is shifted by approximately $k/2a$. In the case of the (220) peak of the Au NP sample this corresponds to a temperature difference of roughly 8 °C. Therefore, it is important to fit Au and SiN$_x$ separately instead of simply determining the peak positions of the yellow curve.

The SiN$_x$ background can be fitted with a sum of 3 or more Gaussians. Due to their very broad shapes (see Fig. 3.10), the parameters of these individual Gaussians can vary greatly and still result in a seemingly good overall fit. It is therefore difficult to determine the "true" configuration of parameters. Furthermore, for each new image, the non-linear least-squares fitting routine may fall in another local minimum and give a slightly different variation of Gaussians. Additionally, the SiN$_x$ has a nonzero - yet very small - thermal expansion coefficient of its own and therefore also changes with temperature.

To tackle the challenges described above, we need a fitting routine that limits the parameter variation and leaves little room for the fit to fall into a local minimum. Python's `lmfit` provides options to set limits for each parameter and it provides a detailed fitting report that allows us to optimally fine-tune the parameters [19].

After a few rounds of trial and error, the fit parameters can be narrowed down and it is ensured that the routine converges for radial profiles of all temperatures. In Figure 3.10 we see the individual parts of the profile we obtained: The sharp Au peaks, fitted with Lorentzians, and the contribution of the membrane, consisting of 4 Gaussians. The (220) Au peak is the one least affected by the background and adjacent Au peaks and gives the most signal. Therefore, we can consider it to be the most reliable. Moving forward, we will use the (220) peak for the evaluation of the thermal expansion of the nanoparticles.
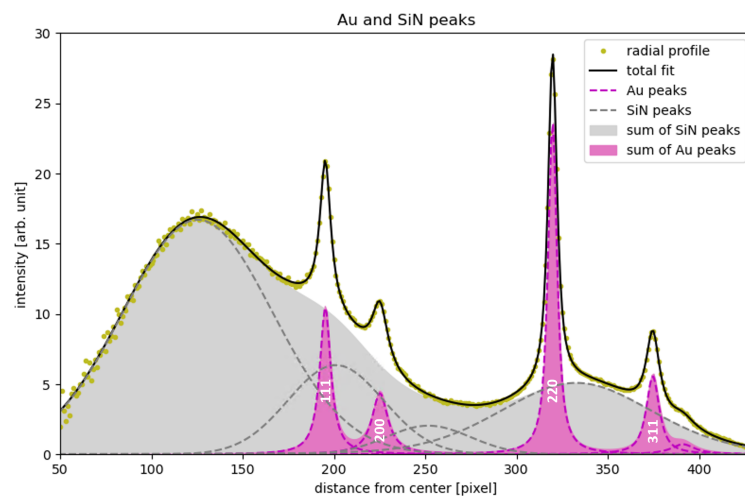
Figure 3.10.: Fits of the Au peaks and the background from the SiN$_x$ membrane.

4. Experiments

4.1. Equipment

All measurements have been performed using a *FEI Tecnai 12* operated at an acceleration voltage of 120 kV. For image recording, it features a *Gatan(R) BioScan* CCD camera with a resolution of 1024×1024 pixels. All diffraction patterns were taken at dwell times between 0.1 s and 1 s.

The *DENSsolutions Wildfire* heating system, which has already been described in Chapter 2, consists of *Nano-Chips* and the corresponding heating holder, with the temperature stimulus controlled and read out via the software *Digiheater*. The *Nano-Chips* have round and oblong windows and are covered with a <20 nm thick amorphous SiN_x membrane that serves as substrate (see e.g. Fig. 4.3) for samples that need to be deposited. The specifications of the heating system are listed in Table 4.1.

Table 4.1.: *Wildfire* heating system specifications [20]

Nano-Chips	D6
heating holder	DH30
Digiheater version	3.2
window size	$ø = 8\,\mu m$
temperature range	$RT - 1,300°C$
T stability	$\pm 0.005°C$
T accuracy	$> 95\%$
T uniformity	$> 99.5\%$
z-displacement $(T < 500°C)$	$< 200\,nm$

The PBED measurements in this thesis were performed based on the work of Niekiel et al. [1]. The high-end 300 kV TEM used there has a condenser lens system consisting of three lenses. The parallel beam can thus be adjusted via the relative excitation of the second and third lenses (C2/C3 zoom). In contrast, with the *FEI Tecnai 12* we only have two condenser lenses and also a camera with lower resolution. On the other hand, we use a newer generation of *Nano-Chips* that exhibit less bulging at high temperatures. We therefore do not have to expect such large z-height changes that affect the ring radii

of the DP, which in turn improves the accuracy of the PBED temperature measurement.

4.2. Sample preparation

As discussed in Section 2.3.2, Au and Ag are most promising for the application of PBED temperature measurements. For the preparation of nanoparticles, we use the dewetting routine: A layer of the material is sputtered onto the back of the *Nano-Chip* which is then heated under continuous observation until nanoparticles form. For this procedure to work, the initial sputter layer must be sufficiently thin, and the temperature must be kept well below the melting point, as the nanoparticles can volatilize at high temperatures due to increased mobility.

Since the very first attempt to make nanoparticles failed, we can demonstrate here what happens when the sputter layer is chosen too thick:

In Figure 4.1 we see how a 20 nm thick Au layer behaves during heating: Here, no nanoparticles are formed - only the grain size changes and stress is induced, as indicated by the black fringes. In contrast, in Figure 4.2, we can see how a 5 nm thick Au layer transforms into free-standing roundish particles. A clear difference can already be observed at room temperature: While the thicker layer covers the membrane continuously, the 5 nm thick layer has formed branched Au islands.

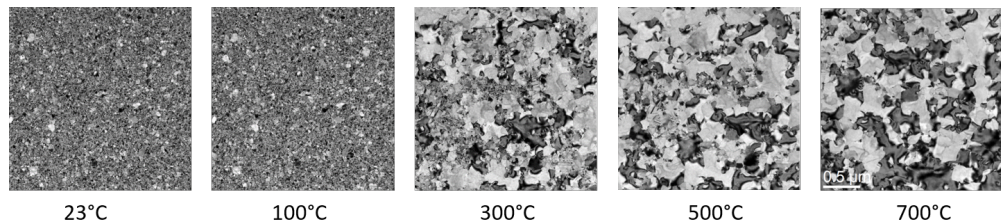| 23°C | 100°C | 300°C | 500°C | 700°C |

Figure 4.1.: Failed dewetting: A 20 nm Au layer is too thick to produce nanoparticles.

Therefore, we choose a nominal thickness of the sputtered layer of 5 nm for both the Au and Ag samples, resulting in nanoparticles with a diameter of 10 to 70 nm that are well distributed across the electron-transparent windows (Fig. 4.3).

Over the course of several experiments with the same sample of Au NP, the particle density on the membrane decreased only slightly, proving its

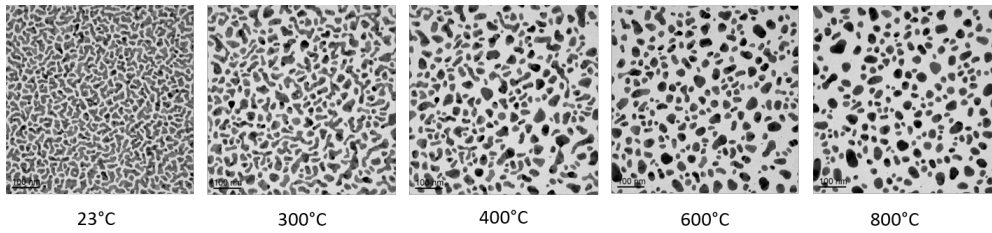23°C   300°C   400°C   600°C   800°C

Figure 4.2.: Formation of Au NP from a 5 nm thick layer with rising temperature.

durability.

Another interesting observation was that in the process of dewetting, the exposure to the electron beam in imaging mode had an effect on NP formation. In Figure 4.4 we see very unevenly sized Ag NP in the area where the beam was directed during the initial heating of the sample.
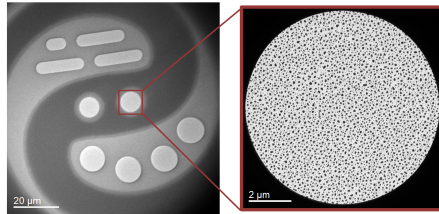

Figure 4.3.: **left**: center of the heating spiral **right**: zooming into one of the circular windows we see the nanoparticles evenly distributed over the entire area

FIB lamella

The final measurement, which will be discussed in detail at the end of Chapter 5, is a proof-of-concept measurement, where we want to show how PBED can be used in an *in-situ* heating experiment. For this purpose, a chip is sputtered with Au and dewetted to obtain Au NP as described previously. Afterwards, a window is cut free from the membrane with a focused ion beam (FIB) (*Thermo Fischer Scientific Ltd.* FIB Nova 200). An electron-transparent lamella of the sample to be examined is then placed in/over this window (see Fig. 4.5). We are using a lamella of an additively manufactured specimen from an AlSi$_{10}$Mg alloy powder [21]. It is cut out with the FIB and has a thickness of about 90 nm.
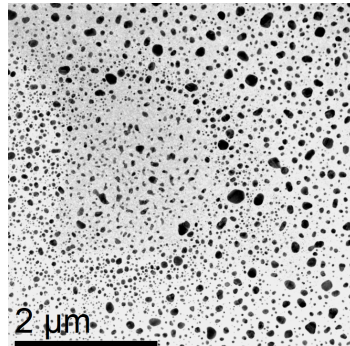
Figure 4.4.: In the presence of the electron beam, the NPs have different shapes and size distributions. We can roughly see the outline of where the electron beam hit the sample during dewetting.
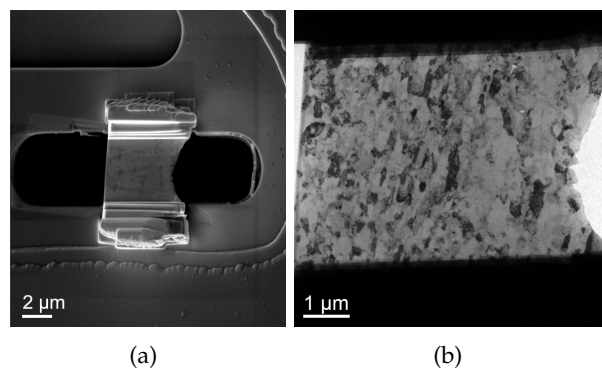

(a)   (b)

Figure 4.5.: The AlSi$_{10}$Mg lamella attached to one of the oblong windows of the *Nano-Chip* in the (a) SEM and (b) TEM.

4.3. Tuning procedure for a parallel beam

In preparation for the PBED measurement, the microscope must be aligned to achieve a parallel electron beam as discussed in Section 2.3.1.

To do this, we first look at which lenses of the microscope affect the beam in front of the specimen. In Figure 4.6 we see a simplified ray diagram of the *FEI Tecnai 12* TEM in diffraction mode. Above the sample we have two condenser lenses, a mini condenser lens, and the upper part of the objective lens.

The first condenser lens (C1) can be controlled by changing the "spot size". It forms an image of the source, that is, in turn, imaged by the second condenser lens (C2) to form the object for the mini-condenser-lens. The latter cannot be adjusted separately. For a fixed spot size the convergence angle β is therefore controlled by both the C2 lens and the objective lens. However, in diffraction mode the objective lens cannot be adjusted either and therefore, we must make sure that the value of the objective lens is always the same before switching to diffraction mode. The condenser aperture sits inside the C2 lens, limiting the angular width of a focused beam and the spatial width of a diverging beam.

To find out whether the beam is convergent, divergent or parallel for a certain combination of settings, a calibration experiment is performed:

We use a 10 nm thick polycrystalline gold foil sample that provides a clear circular diffraction pattern. After setting the eucentric height z_{euc}, the sample is moved to different z-heights, at each of which a DP is recorded. The evaluation of these DPs will show an increase or decrease of the ring radii through the z-height series, which will tell us whether the beam converges or diverges. To reach beam parallelity, we need to vary the C2 currents, while keeping the values of the objective and C1 lens fixed.
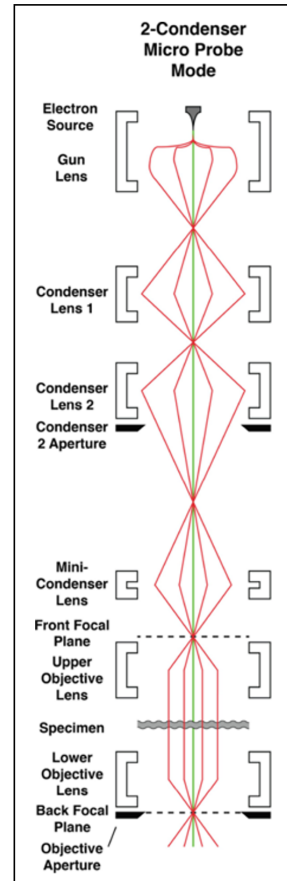

Figure 4.6.: Ray diagram parallel beam. Reprinted from [22] with permission from *Springer Nature*.

29

A potential pitfall of this method is that the ring diameters will only change very little with z-height when the diffraction pattern is not in focus. Thus, if the DP is out of focus, we may mistakenly think that the settings were found for a parallel beam. We therefore have to focus the DP with the diffraction lens at the very beginning and then keep this setting for the rest of the experiments. All TEM settings as used in this measurement can be found in Table 4.2. In

Table 4.2.: TEM settings for the alignment of the beam

sample	polycrystalline Au foil, 10 nm thick
C2 aperture	No. 4 (ø = 30 µm)
objective aperture	No. 3 (ø = 40 µm)
SAD aperture	No. 3 (ø = 200 µm; on the sample: ø = 5.77 µm)
objective lens	93.4014 %
diffraction lens	33.586 %
set camera length	1.5 m
C2 lens	49 %, 50 %, 50.5 %, 50.9 %, 52 %
Δz [relative to z_{euc}]	−20 µm, −10 µm, 0 µm, 10 µm, 20 µm

Figure 4.7 we see how the relative ring radii change with z-height (given relative to the eucentric height; a negative z-height means the sample was above z_{euc} a positive z-height means it was below). From this we can conclude that the electron beam is divergent at low C2 lens currents and convergent at higher currents. There is also an obvious correlation between the slopes of the lines in Figure 4.7 and the lens current. Therefore, we can easily interpolate to that lens current with which we obtain a slope of zero - and thus a parallel beam (Fig. 4.8)
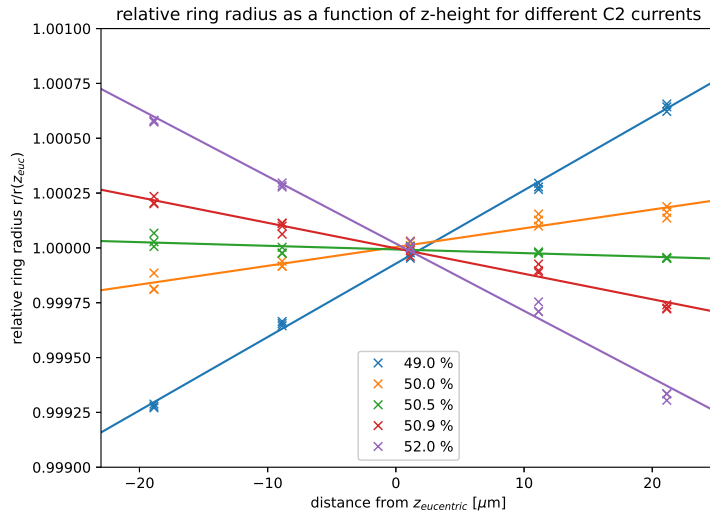
Figure 4.7.: Change in ring radii over the z-displacement from the eucentric height for different C2-lens currents.
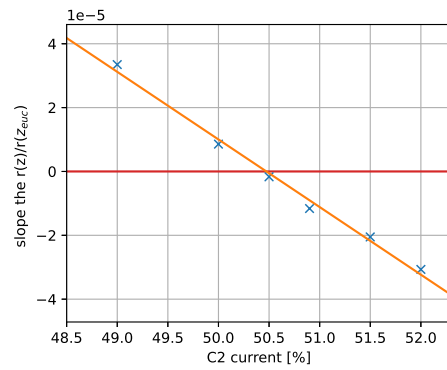

Figure 4.8.: The linear relation between the C2 current and the slopes in Fig. 4.7 can be fitted to obtain the C2 current for a parallel beam ($C2_{parallel} \approx 50.5\,\%$).

4.4. The PBED measurement

4.4.1. Testing suitable materials

To investigate the applicability of a material for this method, we measure its linear thermal expansion and compare it to literature values, e.g., from [23]. Therefore, we record DPs for different T_{set} (temperature we set for the heating system). A reference diffraction pattern is taken at a low temperature where the 5 % error of the heating system is not yet significant. The relative contraction of the diffraction rings $\frac{r_0}{r(T_{set})}$ is then plotted over T_{set}, and the slope gives us the linear expansion coefficient α of the material (see Eq. (2.4)). If the relation is linear and the expansion coefficient matches its literature value within the 5 % error of T_{set}, we have found a reliable material for the temperature measurement. The TEM settings used for these experiments are listed in Table 4.3.

Table 4.3.: TEM settings for PBED

C2 aperture	No. 4 (ø = 30 μm)
objective aperture	No. 3 (ø = 40 μm)
SAD aperture	No. 3 (ø = 200 μm; on the sample: ø = 5.77 μm)
C2 lens	50.9000 %
objective lens	93.4014 %
diffraction lens	33.586 %
set camera length	1.5 m

4.4.2. Application in a heating experiment with a FIB lamella

The lamella we want to investigate is attached to the heating chip as previously described (Section 4.2). Again, a reference diffraction pattern is taken at a low temperature.
We proceed with the heating experiment as we would for any sample. If interesting changes occur, or if we simply want to know the temperature at this moment, we can switch to diffraction mode (settings according to Tab. 4.3) and go to one of the windows covered with nanoparticles to record a DP. The evaluation then shows what temperature prevailed at that time according to PBED.
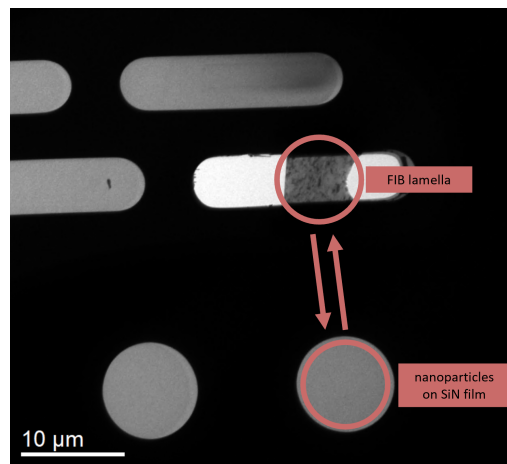
Figure 4.9.: For acquiring a diffraction image for the PBED temperature measurement, we need to move to one of the windows with nanoparticles on them.

5. Results and Discussion

In this chapter we will look at the results of all the heating experiments and discuss the difficulties we encountered, especially with regard to *Nano Chip* calibration.
We will examine the performance of Au and Ag nanoparticles as nano-thermometers for the PBED temperature measurement and discuss its accuracy and possible pitfalls of the evaluation. Finally, we will put its application in a heating experiment to a test, where we investigate the morphological changes in a AlSi$_{10}$Mg FIB-lamella sample at different temperatures.

5.1. The importance of *Nano-Chip* calibration

With our first heating experiments we tried to determine the thermal expansion coefficient of Au nanoparticles following the procedure described in Section 4.4.1. When plotting the relative contraction of the diffraction rings $\frac{r_0}{r(T_{set})}$ against T_{set} we expect to see a linear relation, with the slope being the linear thermal expansion coefficient α (see Eq. (2.4)).

In Figure 5.1 we see the results of the first measurement on Au nanoparticles. While the data points clearly confirm a linear expansion, its slope is much lower than the expected literature value of $\alpha_{lit} = 14.2 \times 10^{-6}\,\mathrm{K}^{-1}$, which cannot be explained by the 5 % error of T_{set}.

There are two possible explanations for the error in the proportionality constant α: Either the material - in our case the Au nanoparticles - does not expand as much as anticipated or the indicated temperature T_{set} of the heating system is incorrect. We first looked into the possibility that nanoparticles behave differently than bulk gold when heated because of size effects. However, the literature did not support this assumption [24],[25] and also, in the work of Niekiel et al. [1] no such size effects were observed. Furthermore, when we repeated the experiment on a different *Nano Chip* we got $\alpha = 17.6 \times 10^{-6}\,\mathrm{K}^{-1}$
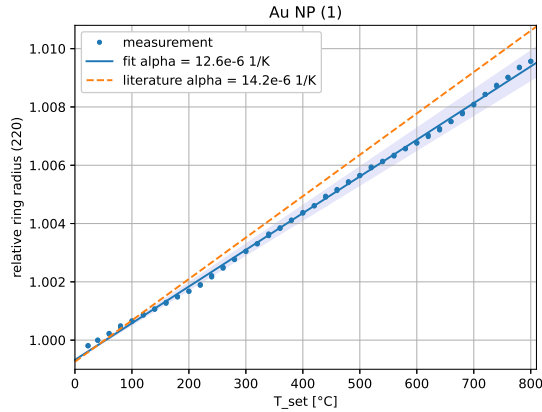
Figure 5.1.: Thermal expansion of Au nanoparticles (sample 1). The light blue area marks the $\pm 5\%$ error region of T_{set}, which clearly does not enclose the orange dashed line of α_{lit}. The (220) ring radius at $T_{set} = 40°$ was taken as reference.

which contradicts the earlier experiment (Fig. 5.2). It thus became evident that the deviations most likely had something to do with the heating system.

As described in Section 2.1, the *Nano-Chips* are calibrated by the manufacturer and delivered in boxes on which the calibration factor b is indicated (Fig. 2.2). We must assume that this factor applies to all chips of that box because they are from the same production batch. However, if the calibration factor b is inaccurate, the temperature we set for the heating system will deviate from the actual temperature of the heating spiral. This error increases linearly with temperature, as we can see from the Callendar-Van Dusen equation (Eq. (2.1)).

In the present case, we suspect that at some point chips from different boxes were mixed up, resulting in us using the wrong calibration factor for several measurements. A closer look at the chips used under the light microscope (Alicona Infinite Focus) supports this assumption: The *Nano Chips* do indeed look differently and their resistance at room temperature also varies greatly. These two observations also suggest that they could come from different production batches.

These circumstances shed light on a different application of the PBED measurement, namely using it to (re)calibrate the chip. To do this, we must of course assume that the expansion coefficient of the nanoparticles matches the literature value. In that manner, the previous measurements can now be
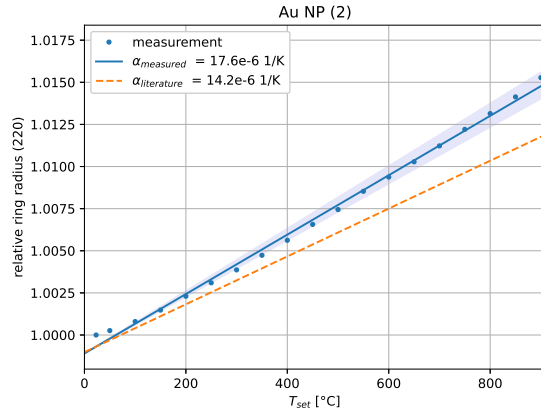
Figure 5.2.: Thermal expansion of Au nanoparticles (sample 2). This time the measured thermal expansion coefficient is clearly larger than α_{lit}.
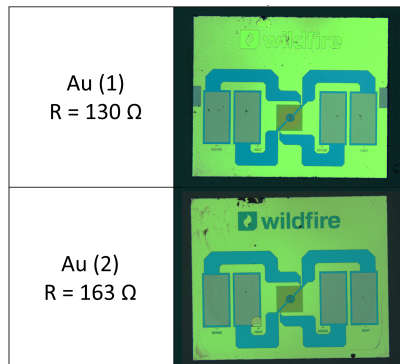

Figure 5.3.: The side-by-side comparison of the used *Nano Chips* reveals that they have slightly different features in branding and layout. Also, their resistance at room temperature differs more than what would be expected from chips from the same production batch.

recalibrated by calculating the temperature from the relative ring radius using Equation (2.4) with α_{lit}. In Figure 5.4 we see that between T_{set} and T_{PBED} there is a temperature difference of up to almost $100°C$ in the first measurement! This situation vividly underlines the importance of well-calibrated heating chips.
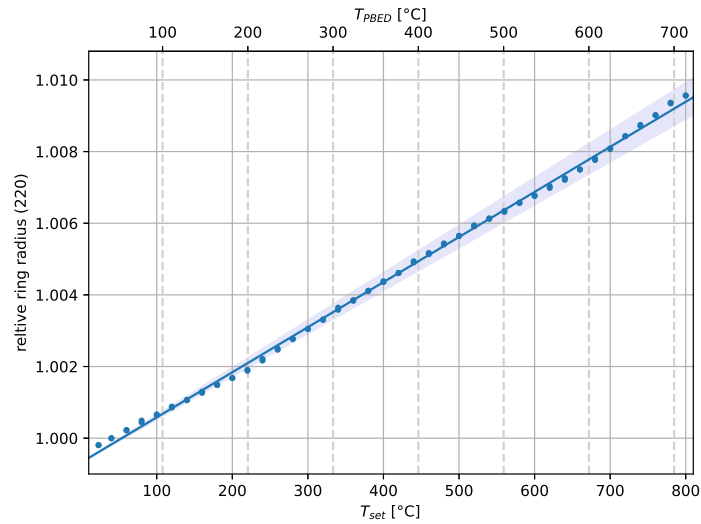

Figure 5.4.: Au NP (1): Comparison of the temperatures according to the heating system T_{set} and the temperatures calculated from the PBED measurement using $\alpha = \alpha_{lit}$.

5.2. Au and Ag nanoparticles

After obtaining misleading results from the mixed-up *Nano-Chips*, we wanted to repeat the experiments with correctly calibrated chips to better evaluate the performance of the PBED temperature measurement. This time we took a very close look at the *Nano-Chips* and their resistance at room temperature beforehand (Fig. 5.5). The variation in the resistance of the chips at room temperature is much lower than for the previously used chips.

To find out if there is a link between the slight deviation of the b-value to the differences in resistance, we conduct the Au measurement on three chips with different resistances (No. 1, 4 and 5). We will also perform a measurement with Ag nanoparticles (No. 7).

Figure 5.5.: Overview of the *Nano-Chips* from the new box with their resistance at room temperature. Chips No. **1, 4, 5**: Au nanoparticles; No. **7**: Ag nanoparticles; No. **6**: Au nanoparticles & FIB-lamella.

The experiments were again conducted following the procedure described in Section 4.4.1. This time, we got results that agree well with the literature expansion coefficients (Figures 5.6, 5.7 and 5.8). Taking a closer look, it seems there is indeed a relation between the resistance of the chip at room temperature and its (correct) b-value.

The increase in α_{meas} for a higher resistance of the chip at RT indeed suggests that there is a relation. The increase of α_{meas} for a higher resistance of the chip at RT indeed indicates a correlation, which however is still within the 5 % uncertainty of the heating system.
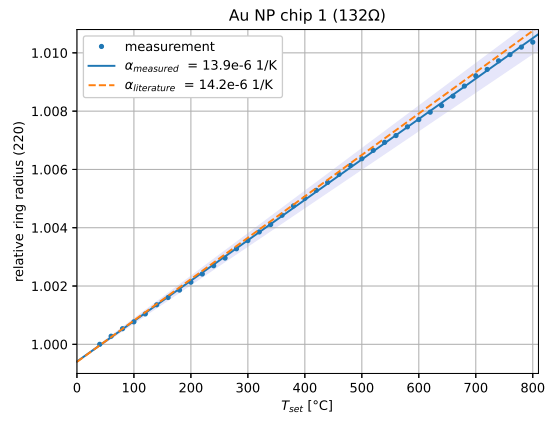
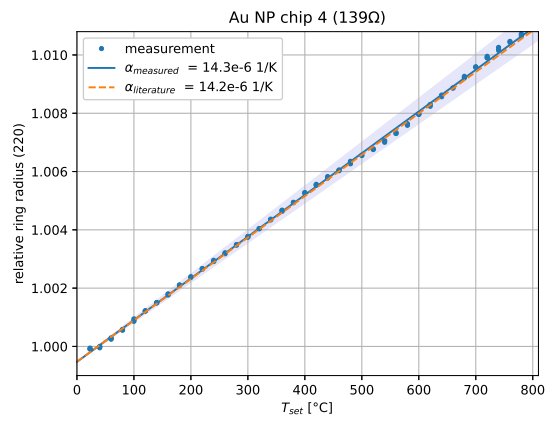Figure 5.6.: Measured thermal expansion of Au NP on chip 1.

Figure 5.7.: Measured thermal expansion of Au NP on chip 4.
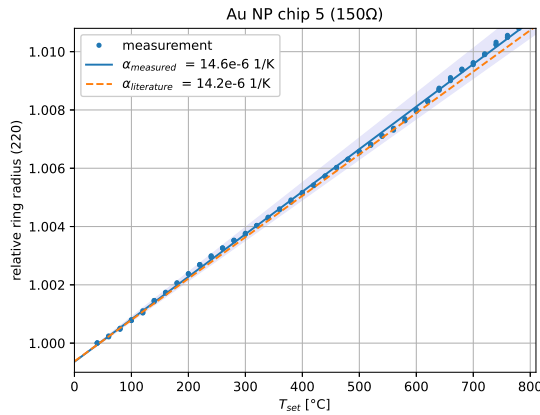
Figure 5.8.: Measured thermal expansion of Au NP on chip 5.

For each temperature, 3-5 diffraction images were taken and evaluated. If we now look at the evaluated data, these measurement points are mostly congruent. At the same time, however, we see somewhat of a periodic deviation around the fit with increasing temperature. Within the examined temperature interval the ring radius of the (220) ring of Ag changes by approximately 4 pixels. This suggests that this deviation originates from the discrete nature of the diffraction pattern, that cannot be fully overcome with the used fit routine.

We see this effect even more pronounced in the measurement with Ag nanoparticles (Fig. 5.9). As discussed in the previous chapter, we used the same nominal thickness for the initial sputter layers of Au and Ag, respectively. For Ag we ended up with a lower nanoparticle density on the membrane. Thus leading to grainier diffraction patterns, which consequently leads to a more inaccurate evaluation of the ring radii.
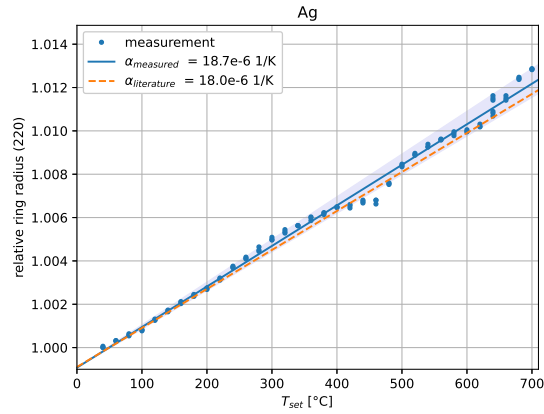
Figure 5.9.: Thermal expansion of Ag nanoparticles.

5.2.1. AlSi10Mg lamella

In the final experiment, the PBED temperature measurement is applied in the context of a typical *in situ* heating experiment.
Prior to attaching the actual sample as a FIB-lamella to the *Nano Chip*, the thermal expansion of the Au nanoparticles was measured. Just like in the previous experiments the slope agreed with the literature value of gold (see Fig. 5.10).
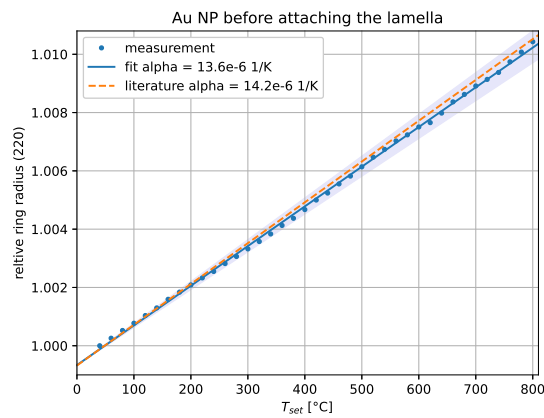
Figure 5.10.: Thermal expansion of the Au NP before further preparation in the FIB.

The lamella was then placed over a window of the *Nano Chip* that had been

cut free from the SiN$_x$ membrane. The heating experiment was conducted as follows: Starting at 40 °C the temperature was gradually increased by 20 °C. At each temperature step images of the lamella were recorded, as well as DP of the Au nanoparticles (Window No. 1 in Fig.5.13).
At 370 °C, cracks began to appear in the lamella, and the temperature was lowered again (Fig. 5.11).

(a) 40 °C   (b) 370 °C

Figure 5.11.: At $T_{set} = 370$ °C the lamella started to crack.

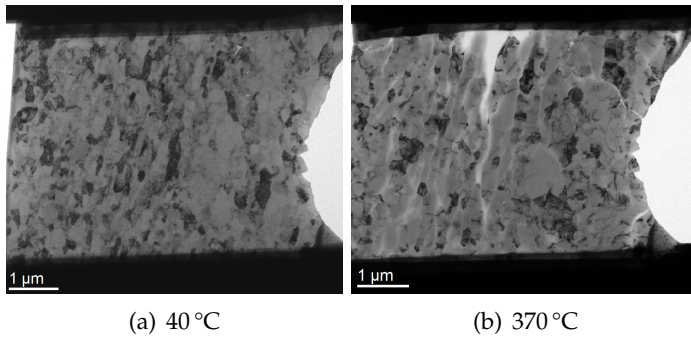Surprisingly, the evaluation of the Au diffraction images now showed a much lower expansion coefficient than before the lamella had been attached. In Figure 5.12 we see both measurements in comparison. It has to be emphasized, that both measurements were conducted on the same exact *Nano Chip*. All microscope settings were the same and also the density of the nanoparticles has not changed. The only difference is that the chip was in the FIB for the attachment of the lamella in between the measurements. We then examined the sample for possible impurities, but could only detect very low concentrations of carbon, which do not explain this deviation.

We repeated the measurement on three different locations/windows of the *Nano Chip*, which are labeled in Fig. 5.13.

The results confirmed the earlier result of $\alpha_{meas(1)} = 10.2 \times 10^{-6}$ K^{-1} in window 1. For windows 2 and 3 we got $\alpha_{meas(2,3)} = 10.9 \times 10^{-6}$ K^{-1} (Fig. 5.14).
Again we are faced with the problem that the measured thermal expansion coefficient does not correspond to the literature value. This time it is particularly odd, because according to the first measurement (before attaching the lamella) we are using the correct calibration factor.
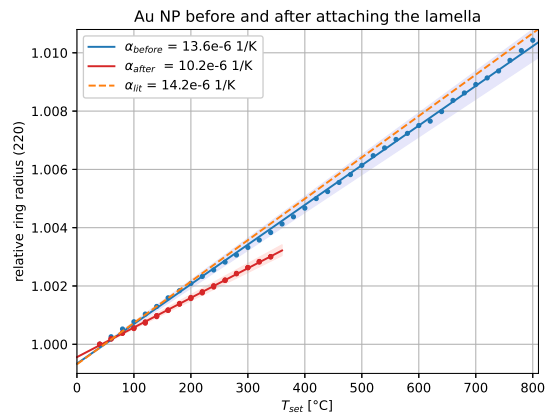What remains unclear, however, is what happened in between the contradicting measurements.

Figure 5.12.: Comparison of the measured relative ring radius as a function of T_{set} before and after attaching the lamella to the Nano Chip.
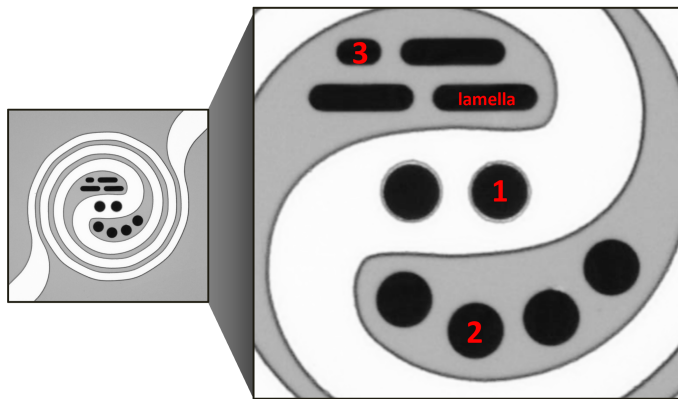

Figure 5.13.: Close-up of the heating spiral and the electron transparent windows of the *Nano Chip*. The PBED measurement of Au NPs was conducted at locations 1, 2 and 3.
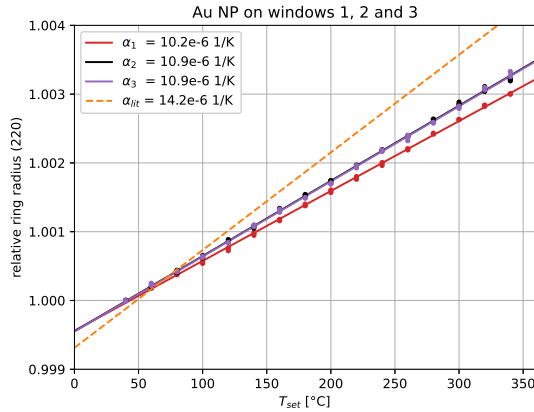
Figure 5.14.: The measurements of α of Au NP on three different locations (see Fig. 5.13) compared to each other and the literature value of bulk gold.

If we assume the PBED measurement of the Au nanoparticles to be correct, the resistance of the heating spiral must have changed in the meantime. If the wire would for example have a crack somewhere, the reduced cross-section at this point would increase the resistance. This would change the proportionality factor between resistance and temperature in the Callendar-Van Dusen Equation. Consequently, we would again be dealing with a "wrongly" calibrated *Nano Chip*. Taking a look at the chip under the light microscope reveals that there is indeed some sort of either damage or redeposition stemming from the FIB sample preparation on the spiral (Fig 5.15).

It is unclear whether this slight damage of the heating coil actually has a noticeable effect on the resistance of the chip. The fact that the resistance at room temperature remained the same, speaks against this assumption.

On the other hand, if we assume that the thermal expansion coefficient of the Au nanoparticles still matches the literature value of $\alpha_{lit} = 14.2 \times 10^{-6}\,\mathrm{K}^{-1}$, we must assume that the chip has been altered in some way so that the previous calibration factor no longer fits. In Figure 5.16 we see the temperatures according to the PBED measurement compared to T_{set}.

Thus, according to the PBED measurement, the white streaks in the lamella would have already appeared at 280 °C degrees instead of at 370 °C.

45
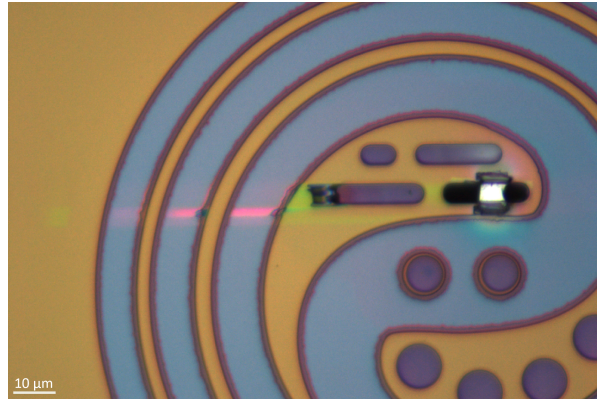
Figure 5.15.: Close-up of the *Nano Chip* in the light microscope. In the course of fixing the lamella to the chip, the heating spiral was apparently damaged, as can be seen from the pink strikes through the wire.
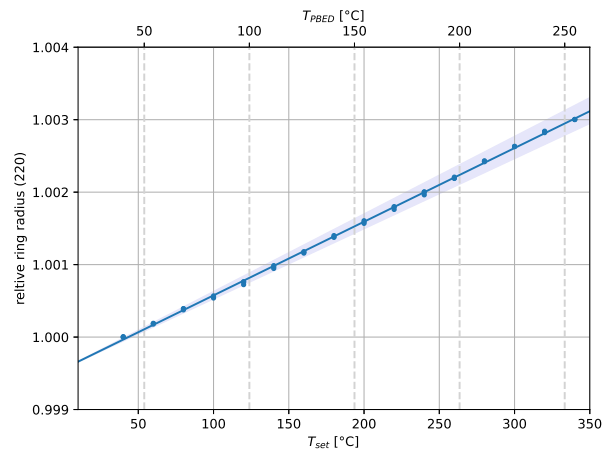
Figure 5.16.: Au NP on window 1: Comparison of the temperatures according to the heating system T_{set} and the temperatures calculated from the PBED measurement using $\alpha = \alpha_{lit}$.

It would have been interesting to monitor the ring radii of the Al islands within the lamella, to see if we can get a PBED measurement of Al after all. However, as the crystallization progresses with temperature, the diffraction pattern of the lamella gets increasingly sparse (Fig. 5.17). This confirms our earlier assumption that thin layers are less suitable for PBED measurements.

(a)   (b)
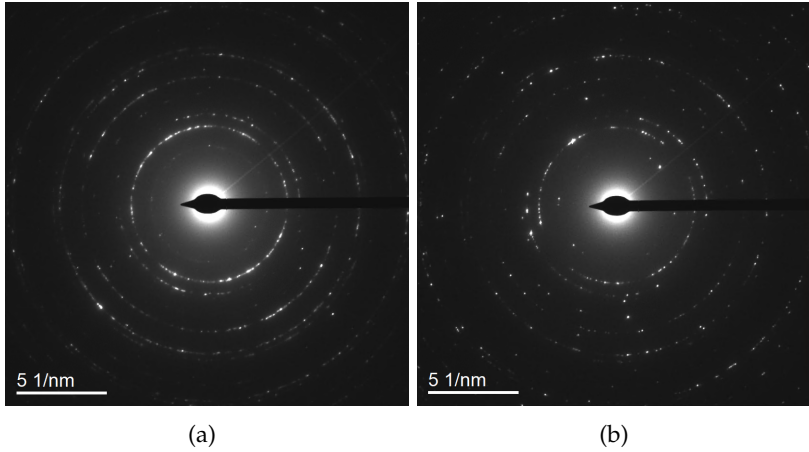
Figure 5.17.: (a) DP of the lamella at room temperature and (b) after heating it up to 370 °C several times.

5.3. Performance of the PBED measurement

The PBED measurements of samples with Au nanoparticles were in good agreement within the error range of the heating system.

At this point we have to separate the discussion of the error into statistical and systematical error. First we will discuss the statistical part: Assuming we have a perfect heating system and that the nanoparticles expand exactly like described by the literature value, we are left with a stochastic error that amounts to 6 -10 °C. This means that with the used evaluation algorithm we are able to determine the radius of the (220) diffraction ring to an accuracy of 0.04 pixel.

The stability of the evaluation scheme was put to the test by recording 30 subsequent diffraction patterns at 800 °C and determining the standard deviation of the resulting ring radii. In this case we found that the standard deviation was only 1.5 °C. This suggests that the difference between the two stochastic errors is caused by the discrete nature of the data (pixel error).

If we assume that the beam parallelism has no significant influence thanks to the alignment performed, there are two effects that contribute to the systematic error of the measurement. Firstly, the uncertainty of the used heating system and secondly, the uncertainty as to whether the observed material actually expands according to the reference from literature.

6. Conclusion

The aim of this master thesis was to extend the applicability of the PBED temperature measurements as shown in [1] to a TEM equipped with 2 condenser lenses and a lower resolution camera.

To pave the way for an accurate measurement, it is crucial to align the microscope to achieve a parallel electron beam. This was realized in a preparatory experiment, using a polycrystalline sample that was moved up and down in the TEM column to find the lens settings where the diffraction rings do not change.

The materials tested were Au and Ag, respectively. These were applied in the form of nanoparticles to the *Nano Chips* by means of solid-state dewetting of a thin sputter layer.

A central role in this work is played by the evaluation algorithm that determines the center of the diffraction pattern with high sub-pixel accuracy and subsequently extracts the radii of the relevant diffraction rings by a fitting routine. The results are then converted to a relative temperature change. The stochastic error of this evaluation method amounts to remarkable 6 °C for the PBED measurement of Au nanoparticles.

By determining the relative expansion of the nanoparticles as a function of the temperature indicated by the MEMS heating system, we calculated their thermal expansion coefficient and compare it to the literature value. This allowed us to find out that the chips used at the beginning were labeled with the wrong calibration factor. For well-calibrated chips, we found excellent agreement with the literature value within the 5 % error of the set temperature. Here we were able to see slight deviations from the calibration factor of the *Nano Chips* within the same production batch.

Finally the method was put to a test in a typical *in situ* heating experiment. Thanks to the PBED measurement, we became aware that the properties of the *Nano Chip* had changed during further preparation steps in the FIB. While the underlying reasons for this change remain a subject of discussion, the PBED measurement clearly suggests that the chip's resistance as a function of the

temperature has been altered and therefore the manufacturer's calibration factor is no longer valid.

In summary, the development of a PBED temperature measurement routine, consisting of the microscope alignment and the evaluation algorithm, has opened the possibility to perform local temperature measurements on TEMs with only 2 condenser lenses. Despite the lower resolution of the camera used, the accuracy achieved is comparatively high due to the precise evaluation algorithm.

Bibliography

[1]   F. Niekiel et al. "Local temperature measurement in TEM by parallel beam electron diffraction." In: *Ultramicroscopy* 176 (2017), pp. 161–169 (cit. on pp. 1, 11–13, 22, 25, 35, 49).

[2]   F. Gaulandris et al. "Methods for Calibration of Specimen Temperature During In Situ Transmission Electron Microscopy Experiments." In: *Microscopy and Microanalysis* 26.1 (2020), pp. 3–17 (cit. on pp. 3, 4, 6).

[3]   DENSsolutions. *Manual: Sample Heating System Double Tilt (30 degrees) DENS-A-DH30-4M-FS* (cit. on p. 4).

[4]   P. Pawlow. "Über den Einfluss der Oberflaeche einer festen Phase auf die latente Waerme und die Temperatur des Schmelzens." In: *Zeitschrift für Chemie und Industrie der Kolloide* 7.1 (1910), pp. 37–39 (cit. on p. 7).

[5]   K.K. Nanda, S.N. Sahu, and S.N. Behera. "Liquid-drop model for the size-dependent melting of low-dimensional systems." In: *Physical Review A* 66.1 (2002), p. 013208 (cit. on p. 7).

[6]   H. Reiss, P. Mirabel, and R.L. Whetten. "Capillarity theory for the coexistence" of liquid and solid clusters." In: *The Journal of Physical Chemistry* 92.26 (1988), pp. 7241–7246 (cit. on p. 7).

[7]   J. Bonneaux and M. Guymont. "Study of the order–disorder transition series in AuCu by in-situ temperature electron microscopy." In: *Intermetallics* 7.7 (1999), pp. 797–805 (cit. on p. 7).

[8]   N. Bayat, T. Carlberg, and M. Cieslar. "In-situ study of phase transformations during homogenization of 6005 and 6082 Al alloys." In: *Journal of Alloys and Compounds* 725 (2017), pp. 504–509 (cit. on p. 7).

[9]   C.J. Martin and J.D. Boyd. "A method for calibrating a specimen-heating stage in the electron microscope." In: *Journal of Physics E: Scientific Instruments* 6.1 (1973), p. 21 (cit. on p. 7).

[10]   E.P. Butler and K.F. Hale. "Dynamic experiments in the electron microscope. Practical methods in electron microscopy." In: (1981) (cit. on p. 7).

[11]   B..C Regan et al. "Introduction to Plasmon Energy Expansion Thermometry." In: *Microscopy and Microanalysis* 21 (2015), pp. 1907–1908 (cit. on p. 8).

[12]   M. Mecklenburg et al. "Nanoscale temperature mapping in operating microelectronic devices." In: *Science* 347.6222 (2015), pp. 629–632 (cit. on p. 8).

[13]   I. Suh, H. Ohta, and Y. Waseda. "High-temperature thermal expansion of six metallic elements measured by dilatation method and X-ray diffraction." In: *Journal of Materials Science* 23.2 (1988), pp. 757–760 (cit. on p. 9).

[14]   K.K. Christenson and J.A. Eades. "Skew thoughts on parallelism." In: *Ultramicroscopy* 26.1 (1988), pp. 113–132 (cit. on p. 10).

[15]   J.P. Winterstein, P.Ann. Lin, and R. Sharma. "Temperature calibration for in situ environmental transmission electron microscopy experiments." In: *Microscopy and Microanalysis* 21.6 (2015), pp. 1622–1628 (cit. on pp. 12, 13).

[16]   D.R. Cremons and D.J. Flannigan. "Direct in situ thermometry: Variations in reciprocal-lattice vectors and challenges with the Debye–Waller effect." In: *Ultramicroscopy* 161 (2016), pp. 10–16 (cit. on pp. 12, 13, 17).

[17]   D. Mitchell. "Circular Hough transform diffraction analysis: A software tool for automated measurement of selected area electron diffraction patterns within Digital Micrograph™." In: *Ultramicroscopy* 108.4 (2008), pp. 367–374 (cit. on p. 16).

[18]   NI IMAQ. "IMAQ Vision Concepts Manual." In: *National Instruments* (2000) (cit. on p. 17).

[19]   M. Newville et al. *LMFIT: Non-Linear Least-Square Minimization and Curve-Fitting for Python*. Version 0.8.0. 2014 (cit. on p. 23).

[20]   DENSsolutions. *Brochure: Wildfire In Situ Heating Systems*. 2020 (cit. on p. 25).

[21]   M. Albu et al. "Microstructure evolution during in-situ heating of AlSi10Mg alloy powders and additive manufactured parts." In: *Additive Manufacturing* 36 (2020), p. 101605 (cit. on p. 27).

[22]   Mark A Herzik. "Setting Up Parallel Illumination on the Talos Arctica for High-Resolution Data Collection." In: *CryoEM*. Springer, 2021, pp. 125–144 (cit. on p. 29).

[23]   Y. S. Touloukian et al. *Thermophysical properties of matter-the tprc data series. volume 12. thermal expansion metallic elements and alloys*. Tech. rep. 1975 (cit. on p. 32).

[24]   C. Solliard and M. Flueli. "Surface stress and size effect on the lattice parameter in small particles of gold and platinum." In: *Surface Science* 156 (1985), pp. 487–494 (cit. on p. 35).

[25]   T. Comaschi, A. Balerna, and S. Mobilio. "Temperature dependence of the structural parameters of gold nanoparticles investigated with EXAFS." In: *Phys. Rev. B* 77 (7 2008) (cit. on p. 35).

Appendices

A. Python Scripts

This section contains the evaluation algorithm, for determining the radii of the (220) diffraction ring of Au nanoparticles sitting on a SiN_x membrane. As described in Section 3.1.3 it consists of two parts: the Peakmax center finder and the fitting routine.

```python
1   #%% packages
2
3   import os #for importing the DP as tiff
4   import matplotlib.pyplot as plt
5   from skimage import io
6   import numpy as np
7   from scipy import signal
8   from scipy.interpolate import griddata
9   from scipy.optimize import curve_fit
10  from lmfit.models import  LorentzianModel, GaussianModel
11
12  #%% functions
13
14  def radial_profile(data, center):
15      # create array of radii
16      x,y = np.meshgrid(np.arange(len(data)),np.arange(len(data)))
17      R = np.sqrt((x - center[1])**2 + (y - center[0])**2)
18      # calculate the mean
19      f = lambda r : data[(R >= r-.5) & (R < r+.5)].mean()
20      r  = np.linspace(1,int(len(data)/2),num=int(len(data)/2))
21      mean = np.vectorize(f)(r)
22      return mean
23
24  def crosscorrelation_kernel(size, r_min, r_max):
25      i,j = np.meshgrid(np.arange(size),np.arange(size),indexing='ij')
26      R = np.sqrt((i - size/2)**2 + (j - size/2)**2)
27      kernel = np.ones([size,size])
```

57

```python
28        kernel[(R < r_min) | (R > r_max)] = 0
29        return kernel
30
31    def peakmax(D, x, r_min, r_max):
32        return np.max(radial_profile(D, x)[r_min:r_max])
33
34    def gauss_2d(x,A,sigma1,sigma2,mu1,mu2,eta,offset):
35        g = A * (1/(2*np.pi*sigma1*sigma2*np.sqrt(1-
36              eta**2)))*np.exp(-(1/(2*(1-eta**2)))*((((x[0]-mu1)**2)/sigma1**2)+
37              (((x[1]-mu2)**2)/sigma2**2)-((2*eta*(x[0]-mu1)*(x[1]-
38              mu2))/(sigma1*sigma2)))) + offset
39        return g.ravel()
40
41    def powerlaw(x, a, k):
42        return a*x**(-k)
43
44    def beamstop_correction(data, center):
45        i,j = np.meshgrid(np.arange(len(data)),np.arange(len(data)),indexing='ij')
46        R = np.sqrt((i - center[0])**2 + (j - center[1])**2)
47        phi = np.zeros([len(data),len(data)])
48        for l in range(len(data)):
49            for u in range(len(data)):
50                phi[l,u] = math.atan2(center[0]-l,u-center[1])
51        phi = phi.ravel()
52        data = data.ravel()
53        R = R.ravel()
54        # deleting data within the slice that inhabits the beam stop
55        beta = 0.070
56        R = R[(phi<-beta)|(phi>beta)]
57        data = data[(phi<-beta)|(phi>beta)]
58        phi = phi[(phi<-beta)|(phi>beta)]
59        # filling it up again with data from the neighboring slice füllen
60        phi_new = np.concatenate((phi,phi[(phi>-3*beta)&(phi<-beta)]+2*beta))
61        R_new = np.concatenate((R,R[(phi>-3*beta)&(phi<-beta)]))
62        data_new = np.concatenate((data,data[(phi>-3*beta)&(phi<-beta)]))
63        # converting the DP back to a matrix
64        j_new = R_new * np.cos(phi_new) + center[1]
65        i_new = R_new * np.sin(-phi_new) + center[0]
66        D_new = griddata((i_new, j_new), data_new, (i,j), method='cubic')
67        D_new[np.isnan(D_new)] = 0
68        return D_new
```

58

```
69
70   def mask(data, center, b_up, b_down, b_noseup, b_nosedown):
71       i,j = np.meshgrid(np.arange(data.shape[1]),np.arange(data.shape[0]),indexing='ij')
72       phi = np.zeros([len(data),len(data)])
73       for l in range(len(data)):
74           for u in range(len(data)):
75               phi[l,u] = math.atan2(center[0]-l,u-center[1])
76       data[(phi>-b_down) & (phi<b_up)] = 0
77       data[(phi < -np.pi + b_nosedown)] = 0
78       data[(phi > np.pi - b_noseup)] = 0
79       #streak
80       a1 = 0.77
81       a2 = 0.63
82       data[(phi> a2) & (phi<a1)] =0
83       return data
```

A.1. Center finding algorithm

```
1    #%% cross correlation
2
3    #  importing the DP as an array
4    path = 'X:\\shared data\\guests\\Verena Fritz\\...' #location of the DP tiffs
5    tifs = os.listdir(path)
6    DP = io.imread(path + '\\' + tifs[0])
7    DP_size = len(DP)
8
9    # inner and outer radius of the kernel ring with reasonable values for
10   # crosscorrelation with the (220) diffraction ring of Au
11   kernel_min = 315
12   kernel_max = 322
13   kernel_size = 700
14
15   cc_kernel = crosscorrelation_kernel(kernel_size, kernel_min, kernel_max)
16   cc_output = signal.correlate(DP, cc_kernel, mode='same')
17   # croping the cross correlation output matrix and determining its maximum
18   cc_red = cc_output[int(DP_size/2-20):int(DP_size/2+20),int(DP_size/2-20):int(DP_size/2+20)]
19   cc_max  = np.where(cc_red == np.max(cc_red))
20   cc_center = [int(DP_size/2-20) + cc_max[0], int(DP_size/2-20) + cc_max[1]]
21
```

```
22
23   #%% peakmax
24   # radius range including the (220) peak
25   r_min = 310
26   r_max = 330
27
28   size_red = 350
29   PM_crop = 3
30   PM_size = 11
31   peak_height = np.zeros([PM_size,PM_size])
32
33   # values for the initual guess of the 2d gaussian fit
34   guess_A = 1300
35   guess_sigma1 = 3
36   guess_sigma2 = 3
37   guess_eta = -0.5
38   guess_offset = 50
39
40   # mask angles
41   mask_lu = 0.3
42   mask_ld = 0.3
43   mask_ru = 0.3
44   mask_rd = 0.3
45
46   # cropping the DP to speed up the subpixel-center finder
47   # and ajusting the cc_center coordinates accordingly
48   DP_size = len(DP)
49   DP_red = DP[int(len(DP)/2-size_red):int(len(DP)/2+size_red),
50              int(len(DP)/2-size_red):int(len(DP)/2+size_red)]
51   cc_center_red = [cc_center[0]-int(len(DP)/2-size_red),
52                    cc_center[1]-int(len(DP)/2-size_red)]
53   # creating a sublattice around cc_center_red (of size +- PM_crop) with
54   # PM_size sites in each direction at each lattice site
55   PM_x = np.linspace(cc_center_red[0]-PM_crop,
56                    cc_center_red[0]+PM_crop, PM_size)
57   PM_y = np.linspace(cc_center_red[1]-PM_crop,
58                    cc_center_red[1]+PM_crop, PM_size)
59   x = np.meshgrid(PM_x, PM_y, indexing = 'ij')
60
61   DP_bcorr = beamstop_correction(DP_red,cc_center_red)
62   # evaluating the peak_height at each lattice site [PM_x,PM_y]
```

```
63  for h in range(PM_size):
64      for j in range(PM_size):
65          peak_height[h,j] = peakmax(DP_bcorr, [PM_x[h], PM_y[j]], r_min, r_max)
66
67  # fitting the peak_height with an asymmetrical 2D Gaussian function
68  # the initial guess was created from trial and error
69  initial_guess=[guess_A,  guess_sigma1,  guess_sigma2,
70                  cc_center_red[0][0], cc_center_red[1][0],
71                  guess_eta,  guess_offset]
72
73  popt, pcov = curve_fit(gauss_2d, x, peak_height.ravel(), initial_guess)
74
75  # the optimal fit parameters popt give us the location of the center
76  center = np.array([popt[3]+int(len(DP)/2-size_red),
77                      popt[4]+int(len(DP)/2-size_red)])
78
79  DP_radial  = radial_profile(mask(DP,center, mask_ru, mask_rd, mask_lu, mask_ld), center)
```

A.2. Fitting routine

```
1   #%% fit routine
2
3   DP_radial  = radial_profile(mask(DP,center, mask_ru, mask_rd, mask_lu, mask_ld), center)
4   r = np.linspace(0.00001, DP_size/2, DP_size/2)
5
6   # specify regions of the DP_radial where the powerlaw should be fitted
7   rpow = np.concatenate((r[53:75],r[430:460]))
8   radpow = np.concatenate((DP_radial[53:75],DP_radial[430:460]))
9   popt_power, pcov = curve_fit(powerlaw, rpow, radpow)
10
11  DP_radial_red = DP_radial - powerlaw(r, *popt_power)
12  DP_radial_red[DP_radial_red < 0] = 0
13
14  # only the region around the (220) peak is fitted
15  r_fit = r[290:350]
16  DP_radial_fit = DP_radial_red[290:350]
17
18  peakAu = LorentzianModel(prefix = 'Au_')
19  pars = peakAu.guess(DP_radial_fit, x=r)
```

61

```python
20   pars.update(peakAu.make_params())
21   pars['Au_center'].set(value = 318, min = 313.5, max = 322)
22   pars['Au_sigma'].set(value = 3.5, min = 1, max = 5)
23   pars['Au_amplitude'].set(min = 0)
24
25   peakSiN = GaussianModel(prefix = 'SiN_')
26   pars.update(peakSiN.make_params())
27   pars['SiN_center'].set(value = 335 , max = 340, min = 333)
28   pars['SiN_sigma'].set(value = 38, min = 20, max = 50)
29
30   model = peakSiN +  peakAu
31   model.eval(pars, x = r)
32   out = model.fit(DP_radial_fit, pars, x = r)
33   comps = out.eval_components(x=r)
34
35   radius_220 = out.best_values['Au_center']
```